Accurate Navier-Stokes Results for the Hypersonic Flow over a Spherical Nosetip

Frederick G. Blottner*
Sandia National Laboratories, Albuquerque, New Mexico 87185

The unsteady, thin-layer Navier-Stokes equations for a perfect gas are solved with a linearized block, alternating direction implicit finite-difference solution procedure. Solution errors due to numerical dissipation added to the governing equations are evaluated. Errors in the numerical predictions on three-different grids are determined where Richardson extrapolation is used to estimate the exact solution. Accurate computational results are tabulated for the hypersonic laminar flow over a spherical body, which can be used as a benchmark test case. Predictions obtained from the code are in good agreement with inviscid numerical results and experimental data.

Introduction

IN the call for papers in a recent AGARD conference,[1] code validation was defined as follows: "Insure that the mathematical and numerical schemes employed in the code accurately model the critical physics of the flowfield." NASA's Ad Hoc Committee on Computational Fluid Dynamics (CFD) Validation of the Aeronautics Advisory Committee has defined CFD code validation as "Detailed surface-and-flow-field comparisons with experimental data to verify the code's ability to *accurately model* the *critical physics* of the flow."[2] The *IEEE Standard Glossary*[3] gives a definition of validation and verification in connection with software quality assurance. A succinct definition of these terms is provided by Boehm[4]: Validation is doing the right job and verification is doing the job right.

Confidence in the predictions produced by a code is obtained by investigating two items, and these are used to define validation and verification as follows:

1) Code validation (*solving right governing equations*) is the evaluation of the accuracy of the governing equations that are being solved. These equations can include assumptions due to using a simplified form of the Navier-Stokes equations or due to modeling required for turbulent flow, transition, real-gas effects, gas-surface interaction, and other flow physics.

2) Code verification (*solving governing equations right*) is the determination of the accuracy of the numerical solution of the chosen governing equations.

To satisfy both of these items is an overwhelming burden to place on the developers of CFD codes. The first item is the responsibility of the fluid mechanics community and is an ongoing research activity. Therefore this paper is concerned mainly with the second item for a Navier-Stokes code called NS3D used for solving the hypersonic perfect gas flow over vehicles with a blunt nose.

The following steps have been taken previously[5,6] to verify the NS3D code: 1) The FORTRAN coding has been carefully checked to insure that it is performing the desired numerical solution procedures. Replacement of subroutines with other independently developed subroutines has not been performed. 2) A careful investigation has been performed to evaluate the sensitivity of numerical solutions to user-specified input parameters. 3) The body surface presure and shock-layer thickness have been compared to inviscid numerical solutions to evaluate the predictions of the present code that are insensitive to viscous effects. The viscous flow predictions of NS3D were evaluated by comparing the heat flux at the stagnation point with boundary-layer predictions. 4) Predictions from the code have been compared to experimental results for surface pressure and heat flux. The comparison to experimental data has been limited to laminar flows and wind-tunnel conditions where the governing equations with the perfect gas assumption are reasonable.

The purpose of this paper is to provide further verification of the Navier-Stokes code NS3D. The main objective of this paper is to provide an accurate solution for a test case that can be used as a benchmark result. The test case is laminar flow over a spherical body at $M_\infty = 5$ at a high Reynolds number. In addition, influence of numerical dissipation and the accuracy of the results are evaluated for the test case. The accuracy of the governing equations are also investigated. Although the code includes a general three-dimensional solution procedure, the present evaluation is concerned only with predictions obtained with the axisymmetric option. More details of the code and results from the code are presented in Refs. 5 and 6.

Navier-Stokes Code

In the code NS3D, the thin-layer form of the unsteady-compressible Navier-Stokes equations are solved. The governing conservation equations are first written in Cartesian coordinates x, y, and z and Cartesian velocity components u, v, and w; then the equations are transformed into curvilinear coordinates. For laminar flow, which is considered in this paper, the conservation equations are completed with the perfect-gas equation of state, Sutherland's viscosity law, and a constant Prandtl number. The basic solution procedure can be applied to general three-dimensional geometries, but the present code has been limited to flow over bodies with a plane of symmetry. In addition, an axisymmetric option is available in the code, which is used in the results presented in this paper. The formulation uses the curvilinear coordinates $\xi = y^1$, $\eta = y^2$, and $\zeta = y^3$, which are defined as follows: ξ is the coordinate along the body surface starting at the nose and axis of the body; η is the coordinate around the body, which measures the distance along the surface from the windward to leeward plane of symmetry; and ζ is the coordinate from the body surface to the shock wave where the body surface is $\zeta = 0$.

This paper is concerned with the use of the NS3D code for the generation of blunt-body solutions on axisymmetric bodies

Presented as Paper 89-1671 at the AIAA 24th Thermophysics Conference, Buffalo, NY, June 12-14, 1989; received July 20, 1989.

*Distinguished Meamber of Technical Staff. Fellow AIAA.

at a zero angle of attack. For this case, a three-dimensional solution is unnecessary, and the governing equations can be reduced to a two-dimensional problem. The thin-layer form of the Navier-Stokes equations is used where the viscous terms with derivatives in the ξ and η are neglected. The ζ coordinate should be normal or nearly normal to the body surface. The axisymmetric thin-layer Navier-Stokes equations become

$$\frac{\partial \hat{Q}}{\partial t} + \frac{\partial \hat{F}^1}{\partial \xi} + \hat{H} + \frac{\partial \hat{F}^3}{\partial \zeta} = Re^{-1}\frac{\partial \hat{G}^3}{\partial \zeta} \tag{1}$$

The dependent variable $\hat{Q} = J^{-1}Q$, and the inviscid flux vectors for $i = 1,2,3$ are

$$\hat{Q} = J^{-1}\begin{bmatrix} \rho \\ \rho u \\ \rho w \\ e \end{bmatrix}, \qquad \hat{F}^i = J^{-1}\begin{bmatrix} \rho v^i \\ \rho u v^i + y_x^i p \\ \rho w v^i + y_z^i p \\ v^i(e+p) - y_t^i p \end{bmatrix} \tag{2}$$

where the variables are nondimensionalized with a reference length L^*, freestream sound speed a_∞^*, freestream density ρ_∞^*, freestream viscosity μ_∞^*, freestream thermal conductivity k_∞^*, freestream specific heat $c_{p_\infty}^*$, and reference temperature $T_r^* = a_\infty^{*2}/c_{p_\infty}^*$. The Reynolds number is defined as $Re = \rho_\infty^* a_\infty^* L^*/\mu_\infty^*$. Contravariant velocities are introduced and defined as

$$v^i = y_t^i + y_x^i u + y_z^i w \tag{3}$$

where $U = v^1$ and $W = v^3$. For a perfect gas, the pressure becomes

$$p = (\gamma - 1)[e - \tfrac{1}{2}\rho u^2] \tag{4}$$

where $u^2 = u^2 + w^2$. The temperature for a perfect gas is obtained from

$$T = [\gamma/(\gamma-1)](p/\rho) = h = \gamma e_i = \gamma[e/\rho - \tfrac{1}{2}u^2] \tag{5}$$

where the ratio of specific heat $\gamma = 1.4$. For the axisymmetric case $r = z$ and $y = 0$, the gradient of the flux vector $\hat{F}^2$ becomes

$$\hat{H} = \frac{\partial \hat{F}^2}{\partial \eta} = J^{-1}\begin{bmatrix} 0 \\ 0 \\ -p/r \\ 0 \end{bmatrix} \tag{6}$$

where $J^{-1} = r(x_\xi r_\zeta - x_\zeta r_\xi)$. In addition, in the evaluation of the stresses and heat conduction terms with the thin-layer Navier-Stokes equations, the velocity and temperature gradients are determined with the chain rule, but the ξ and η derivatives are neglected again. The viscous flux vector $\hat{G}^3$ becomes

$$\hat{G}^3 = J^{-1}\begin{bmatrix} 0 \\ \mu m_1 u_\zeta + m_2(\mu+\lambda)\zeta_x \\ \mu m_1 w_\zeta + m_2(\mu+\lambda)\zeta_z \\ m_1(k/Pr)T_\zeta + \tfrac{1}{2}\mu m_1 (u^2)_\zeta + m_2(\mu+\lambda)m_3 \end{bmatrix} \tag{7}$$

where $m_1 = g^{33} = \zeta_x^2 + \zeta_z^2$, $m_2 = (\zeta_x u_\zeta + \zeta_z w_\zeta)$, and $m_3 = u\zeta_x + w\zeta_z$. The thin-layer Navier-Stokes approximation results in the neglect of longitudinal curvature effects that occur in second-order boundary-layer theory.

For the perfect gas model, it is assumed that the Prandtl number is constant, which gives $Pr = \mu^* c_p^*/k^* = 0.72$. The nondimensional thermal conductivity becomes $k = \mu$ since the specific heat at constant pressure is assumed constant, which gives $c_p = 1$. The viscosity in (kg/m-s) is evaluated with Sutherland's law

$$\mu^* = 1.458 \times 10^{-6} T^{*1.5}/(T^* + 110.4) \tag{8}$$

where the temperature T^* is in degrees Kelvin. The second coefficient of viscosity has been retained and evaluated with Stokes's hypothesis that gives $\lambda = -(2/3)\mu$.

The code has been set up to solve the flow between the body and the shock wave and from the stagnation streamline to some downstream outflow or exit plane where the maximum value of ξ occurs. The code includes boundary conditions appropriate for the foregoing flow situations and are updated after the interior solution has been obtained. The bow shock wave is treated as the outer boundary with shock fitting where the following Rankine-Hugoniot relations are satisfied when the shock wave becomes stationary:

$$\rho_{sh} = (\gamma+1)\theta_{n\infty}^2/[(\gamma-1)\theta_{n\infty}^2 + 2] \tag{9a}$$

$$u_{sh} = u_\infty + B\zeta_x, \qquad w_{sh} = w_\infty + B\zeta_z \tag{9b}$$

$$e_{sh} = p_{sh}/(\gamma-1) + \rho_{sh}u_{sh}^2/2 \tag{9c}$$

$$p_{sh} = [2\theta_{n\infty}^2 - (\gamma-1)p_\infty)]/(\gamma+1) \tag{9d}$$

The normal velocity relative to the shock wave is

$$\theta_{n\infty} = -(u_\infty\zeta_x + w_\infty\zeta_z)/\sqrt{g^{33}} \tag{10}$$

and the parameter B is

$$B = 2(\theta_{n\infty}^2 - 1)/[(\gamma+1)\theta_{n\infty}\sqrt{g^{33}}]$$

At the body surface, the gas velocity is zero ($u = 0$ and $w = 0$), the temperature is specified as $T = T_w$, and the normal pressure gradient is assumed zero. Along the stagnation streamline boundary, the flow properties are extrapolated from the interior flow properties with a second-order-accurate procedure. At the outflow boundary, linear extrapolation of the interior flow properties is used to evaluate the flow properties at the exit plane. In the subsonic region of the boundary layer at the outflow boundary, the pressure is assumed constant and equal to the pressure where the flow is sonic.

As part of the input to the code, the grid points in the physical space must be provided. A uniform grid with step-size $\Delta\xi = \Delta\zeta = 1$ is used with the curvilinear computational coordinates $\xi = j - 1$ and $\zeta = l - 1$ where the indices j and l start at 1 and go to J and L in the two coordinate directions, respectively. The grid points in the physical space are nonuniformly spaced to capture details of the flow. For each grid point (ξ and ζ) the corresponding grid point (x and z) in the Cartesian physical space must be specified.

The numerical technique for solving the blunt body flow uses the linearized block alternating direction implicit (ADI) method with central differences for spatial flux derivatives. Before these equations are differenced the flux vectors in the governing equations are linearized with respect to the dependent variables $\hat{Q}$ as follows:

$$(\hat{F}^1)^{n+1} = (\hat{F}^1)^n + \hat{A}\Delta\hat{Q} \tag{11}$$

where

$$\hat{A} = \partial\hat{F}^1/\partial\hat{Q}$$

$$\Delta\hat{Q} = \hat{Q}^{n+1} - \hat{Q}^n$$

The other linearization matrices $\hat{C}$, $\hat{D}$, and $\hat{M}$ are related to the flux vectors $\hat{F}^3$, $\hat{H}$, and $\hat{G}^3$, respectively. Central differences are used for the spatial derivatives and are evaluated implicitly at the new time level. Spatial derivatives for the inviscid flux vectors are evaluated with central difference relations, and the

following notation is used, for example:

$$\frac{\partial W}{\partial \xi} = \delta_\xi W = (W_{j+1} - W_{j-1})/2\Delta\xi \tag{12}$$

The spatial derivative of the viscous flux vector is evaluated with a midpoint scheme because these terms already contain first derivatives. The midpoint relation is

$$\frac{\partial W}{\partial \zeta} = \bar{\delta}_\zeta W = (W_{l+1/2} - W_{l-1/2})/\Delta\zeta \tag{13}$$

A two-point backward difference is used for the unsteady derivative, and for this difference the time marching parameter $h = \Delta t$ in the subsequent equations. The difference equations are written in delta form, and the unknowns in these equations are $\Delta\hat{Q}$. With the ADI approach, the difference equations are factored into one-dimensional block-tridiagonal problems that are then solved in each of the spatial coordinate directions. For the axisymmetric case, the complete difference relation becomes

$$\left[I + h\hat{D} + h\delta_\zeta \cdot \hat{C} - hRe^{-1}\bar{\delta}_\zeta \cdot \hat{M} - D_i(\zeta)\right]\Delta Q^* = -\Delta t(RHS + D_e) \tag{14a}$$

$$\left[I + h\delta_\xi \cdot \hat{A} - D_i(\xi)\right]\Delta\hat{Q} = \Delta Q^* \tag{14b}$$

where

$$RHS = \left(\delta_\xi \hat{F}^1 + \hat{H} + \delta_\zeta \hat{F}^3 - Re^{-1}\bar{\delta}_\zeta \hat{G}^3\right)^n$$

In the present formulation, numerical dissipation terms are required in the differnce equations to have a stable numerical scheme. Implicit and explicit dissipation terms have been added to the difference equations. The implicit dissipation term is a second difference multiplied by ϵ_i, whereas the explicit dissipation term is a fourth difference multiplied by $\epsilon_e = SMU$, The value of SMU is an input parameter to the code, which must be specified and should be as small as possible while allowing solutions to be obtained. The implicit dissipation term to maintain stability is specified as $\epsilon_i = 3\epsilon_e$. The explicit dissipation term is

$$D_e = \epsilon_e J^{-1}\left[\Delta\xi^4 Q_{\xi\xi\xi\xi} + \Delta\zeta^4 Q_{\zeta\zeta\zeta\zeta}\right]^n \tag{15}$$

The explicit dissipation involves fourth derivatives, and these are written, for example in the ξ direction, as

$$Q_{\xi\xi\xi\xi} = (Q_{j+2} - 4Q_{j+1} + 6Q_j - 4Q_{j-1} + Q_{j-2})/\Delta\xi^4$$

At grid points adjacent to the boundaries, the preceding dissipation term is replaced with a second-order derivative. The steady-state solution for the blunt-body problem is obtained by marching the solution of the difference equations in time until a steady result is obtained. A marching time step or Courant number (CN) must be specified as input to the code. At steady state, the equation $RHS + D_e = 0$ is satisfied, and the steady thin-layer Navier-Stokes equations have been solved with an error due to the dissipation term and the truncation error of the numerical scheme.

A separate algebraic grid generation code has been developed for use with the NS3D code. The code will generate the grid around a sphere or sphere-cone configuration. The x axis is along the body axis whereas the z axis is the radial coordinate for the axisymmetric case. The body grid points are equally spaced along the spherical nose surface. The outer boundary of the grid is the shock wave. A variable grid spacing is employed between the body surface and the outer boundary. There are several grid spacings included in the grid code, but the only one used in the present work is one developed at NASA Ames Research Center. In this technique, the ratio of adjacent grid intervals is specified with an algebraic expression that allows the grid spacing to increase in size away from the wall and become uniform in the outer region. The ratio of adjacent grid intervals, K_l, is expressed as

$$\nabla N_l = K_l \nabla N_{l-1}, \qquad l = 3,4,\ldots,L \tag{16}$$

where

$$\nabla N_l = N_l - N_{l-1}, \qquad N_1 = 0, \qquad N_L = 1$$

$$\nabla N_2 = (N_2 - N_1) = \text{specified quantity}$$

The value of K_l is a function of a scale parameter ϵ, which is determined such that the preceding conditions are satisfied. The NASA Ames approach uses a uniform grid when $l > l_u$, where $K_l = 1$ and $\epsilon = 0$. When $l < l_u$, the grid ratio parameter is

$$K_l = 1 + \epsilon \sin[\pi(l-2)/(l_u - 1)], \qquad l = 3,4,\ldots,(l_u - 1)$$

Besides the total number of grid points L in the normal coordinate direction, the input parameters DFM and PER are used to control the grid spacing. The parameter $DFM = (N_2 - N_1)$ is the step-size at the wall, and is nondimensionalized by the length of the normal coordinate from the body to the shock wave. The parameter PER is the fraction of nonuniform grid points, $PER = l_u/L$.

Sensitivity of Obtaining Steady-State Solution to Input Parameters

Before accuracy of the blunt-body solutions can be evaluated, time independent results must be generated. The influence of the various input parameters on obtaining the steady-state blunt-body solution from the NS3D code has been investigated in Refs. 5 and 6. This part of the paper is concerned with a summary of this previous evaluation.

The convergence of the solution to a steady-state result is judged from the value of the L_2 residual. The residual is the L_2 norm, which is defined as

$$L_2 = \left(\frac{1}{I_g}\sum_{i=1}^{I_g} R_i\right)^{1/2} \tag{17a}$$

and

$$R_i = \sum_{n=1}^{5}(RHS + D_e)^2 \tag{17b}$$

The residuals $(RHS + D_e)$ of the difference equations [see Eq. (14)] for the five steady-state conservation equations are squared and summed at each grid point i to obtain R_i. This new residual is then summed over all interior grid points, where I_g is the total number of interior grid points. At steady-state conditions, the L_2 residual should approach zero.

The laminar flow over a sphere at $M_\infty = 5$ is used as the test case to illustrate the behavior of the solution to variation of the different input parameters. This case is chosen because there are experimental data and inviscid numerical calculations available for code verification. The basic input parameters used for this example are given in Table 1. The reference length R_L is the diameter of the spherical nose. The grid parameters DFM and PER were defined in the preceding section. The

Table 1 Test case conditions

Flow conditions	Numerical parameters
$M_\infty = 5$	$JMAX = 23,45,89$
$R_L = 0.027$ m	$KMAX = 1$
$Re = 1.8875 \times 10^6$	$LMAX = 25,49,97$
$T_w = 178.0$°R	$DFM = 5 \times 10^{-5}$
$T_\infty = 136.1$°R	$PER = 0.6$
	$SMU = 10$
	CN = 80.0

Courant number is defined as $CN = \Delta t\, \sigma_{max}/\Delta s_{min}$ where σ_{max} is the maximum eigenvalue of the governing equations within the solution region and Δs_{min} is the minimum spatial step-size in the computational coordinates.

Grid Parameters

The location of the grid points can influence the accuracy and time-marching convergence of the numerical results. The Cartesian coordinates x, y, and z for all of the grid points are required as input quantities. The number of grid points along the body is determined by $J = JMAX$, whereas the number of points between the body surface and the shock wave is determined by $L = LMAX$.

The present investigation is limited to the grid distribution function N_l defined by Eq. (16), which introduces two input quantities, *DFM* and *PER*. The nonuniform grid spacing is used to give an adequate number of points in the boundary layer, which varies in thickness as the Reynolds number of the flow is changed. For the present test case, $DFM = 5 \times 10^{-5}$ and $PER = 0.6$ are used with $LMAX = 97$. For this case, $l_u = 58$ and $\epsilon = 0.174551$. In the grid refinement studies in the ζ direction, the grid distribution is held fixed with the next coarsened grid obtained by removing every other grid point. The grid with coarse spacing is shown in Fig. 1. The grid distribution function across the shock layer for the case with $LMAX = 25$ is given in Table A1 in Appendix A.

As the grid is made smaller near the surface, the convergence to a steady state is slowed down significantly. The fraction of points that are spaced nonuniformly, *PER*, was varied to investigate the influence on the solution. There is very little influence of *PER* on the convergence of the solution toward a steady state.

Grid Refinement

The test problem has been solved with $JMAX = 23$, 45, and 89. In terms of a polar coordinate system, the angular increments along the body surface for these cases are 5, 2.5, and 1.25 deg, respectively. The rate of convergence of the solution toward a steady state is weakly influenced by the number of grid points along the body surface. Solutions have been obtained with $LMAX = 97$, 49, and 25. The convergence of the solution toward a steady state is slowed down significantly as the number of grid points across the shock layer is increased.

Courant Number

The advantage of an implicit time-marching difference scheme is that the method is stable with a large time step or CN ($CN \gg 1$). This allows a steady-state solution to be obtained with fewer time steps but not a time-accurate result. The appropriate CN for the test case problem has been investigated by obtaining solutions for various values. For each value of CN, the solution is marched in time with CN fixed. As the CN is increased, the convergence rate is improved significantly. However, there is an optimum value of CN, since too large a value slows down the convergence rate. For the present case, the optimum CN is approximately 250.

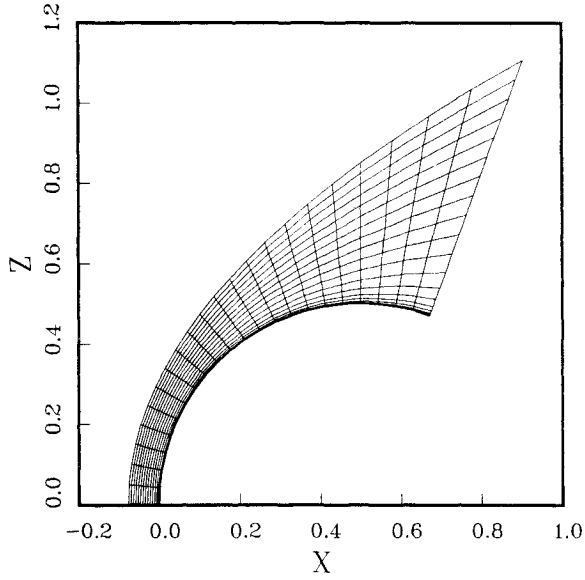

Fig. 1 Coarse grid on sphere: $J = 23$, $L = 25$.

Numerical Dissipation

The present finite-difference scheme uses a dissipation term to stabilize the numerical solution. Results have been obtained with various values of *SMU*, which control the amount of dissipation that has been added. The dissipation coefficient *SMU* has very little influence on the rate of convergence of the solution toward a steady state.

Accuracy of Steady-State Results

The first step in obtaining accurate steady-state numerical results is the selection of an appropriate grid. A uniform grid along the body has been assumed, whereas a variable distribution of grid points between the body and shock wave is allowed. For a fixed number of grid points across the shock layer, one must determine the grid distribution function N_l that provides the most accurate results. In previous work, the parameters *DFM* and *PER* were chosen to give reasonably smooth profiles of the dependent variables in the computational coordinate across the shock layer. With this approach, the finite-difference relations for the derivatives are used to evaluate smooth curves to provide accurate results. Some type of adaptive technique would be desirable to help select the grid spacing. The next step is to minimize the numerical dissipation used in the solutions. Finally, numerical dissipation behavior and grid refinement studies are used to investigate the accuracy of the solutions.

When a steady-state solution has been obtained, the thin-layer, Navier-Stokes equations are approximated as

$$\frac{\partial \hat{F}^1}{\partial \xi} + \hat{H} + \frac{\partial \hat{F}^3}{\partial \zeta} - Re^{-1}\frac{\partial \hat{G}^3}{\partial \zeta} = RHS + D_e + T \tag{18}$$

where T is the truncation error of the difference approximation to the partial differential equations. The exact solution of the partial differential equations, Q_E, is related to the numerical solution of the difference equations, Q_N, and is expressed as

$$Q_E = Q_N + SMU \times D + t \tag{19}$$

where the dissipation and truncation error terms are

$$D = \left[d_1\left(\frac{J_0-1}{J-1}\right)^4 + d_2\left(\frac{L_0-1}{L-1}\right)^4 \right]$$

$$t = a\left(\frac{J_0-1}{J-1}\right)^2 + b\left(\frac{L_0-1}{L-1}\right)^2 + \cdots$$

The number of grid points used in the ξ and ζ coordinate directions with the coarse grid is J_0 and L_0, respectively; the number of grid points used with the refined grids is J and L. The dissipation term D is fourth-order in terms of the step size, and the leading term t in the truncation error is second-order. If *SMU* is held constant as the grid is refined and a steady-state solution is obtained, the numerical solution Q_N approaches the exact solution Q_E. In addition, several solutions with a different number of grid points can be used with Richardson extrapolation[7] to obtain an improved solution with a smaller truncation error. This same approach can be used to evaluate the influence of dissipation on the solution where solutions with various values of *SMU* are required.

Numerical Dissipation

The influence of the dissipation term on the results has been investigated by obtaining solutions with a fixed number of grid

Table 2 Influence of *SMU* on surface pressure and heat flux at $\xi = 90$ deg[a]

Grid	*SMU*	p_w/p_∞	q_w, kW/m^2
$JMAX = 23$	0	1.62258	7.97707
$LMAX = 25$	5	1.61099	7.76188
	10	1.60598	7.97235
	20	1.58938	7.96763
	40	1.56158	7.86627
$JMAX = 45$	0	1.57535	8.27713
$LMAX = 49$	5	1.57453	8.27711
	10	1.57437	8.28781
	20	1.57339	8.29849
	40	1.57137	8.31405
	80	1.56760	8.33694
$JMAX = 89$	0	1.56433	8.42643
$LMAX = 97$	10	1.56427	8.42615
	20	1.56421	8.42587
	40	1.56409	8.42526

[a]L_2 residual $\leq \times 10^{-8}$.

points and for several values of the explicit dissipation coefficient *SMU*. The solution at one grid point location (at the body surface and 90 deg away from the stagnation point) is used as representative of the numerical solution. The results for the pressure and heat flux to the wall at this location are given in Table 2. Since in the present test case the wall temperature is specified, the dependent variables ρ and e are proportional to the pressure p. The pressure results from this table are plotted in Fig. 2. With the coarse grid, the expected linear variation is less accurate. If *SMU* is changed with a fixed grid, the terms Q_E, D, and t remain nearly constant in Eq. (19). With this equation determined for two values of *SMU*, the solution with $SMU = 0$ is determined from

$$Q_N(SMU \to 0) = Q_{N_0} = Q_{N_1} + SMU_1 \times D \tag{20}$$

where

$$D = -(Q_{N_1} - Q_{N_2})/(SMU_1 - SMU_2)$$

In Table 2, the pressure and heat flux have been extrapolated to the case where $SMU = 0.0$ by using the results for $SMU_1 = 10$ and $SMU_2 = 20$. The error percentage of the solution is determined from

$$\% \text{ error of } Q_N = 100 \times [Q_N - Q_{N_0}]/Q_{N_0} \tag{21}$$

This error estimate is presented in Fig. 3 for the pressures p_w/p_∞ given in Table 2. The expected error variation is also given in this figure and is determined from the relation

$$\% \text{ error of } Q_N = 100 \times SMU \times D/Q_{N_0} \tag{22}$$

where D is obtained from Eq. (19) with $(d_1 + d_2) = 0.0016$. This result indicates that the dissipation term introduces a significant error for the coarse grid solution, but the fine grid solution is only slightly in error.

When a similar analysis is applied to the heat flux results presented in Table 2, the results are not as good. It appears that the heat flux requires a finer grid before this type of error analysis can be used effectively.

Grid Refinement

Evaluation of the results obtained from a numerical code with different grids is important for several reasons.

1) The solution convergence behavior with grid refinement should have the properties that are appropriate for the order of accuracy of the numerical scheme.

2) With Richardson extrapolation used to obtain a more accurate result (estimated exact solution), the accuracy of the results can be determined.

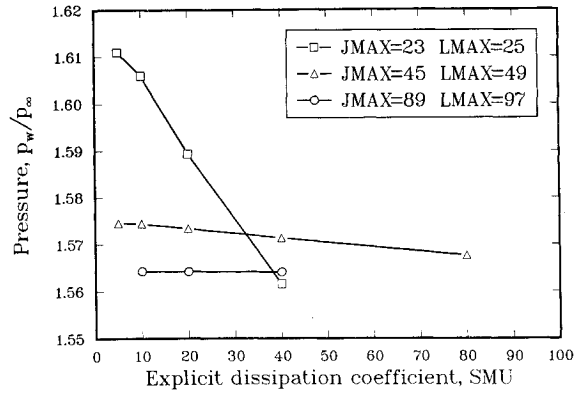

Fig. 2 Variation of the surface pressure p_w/p_∞ with *SMU* at 90 deg around the sphere.

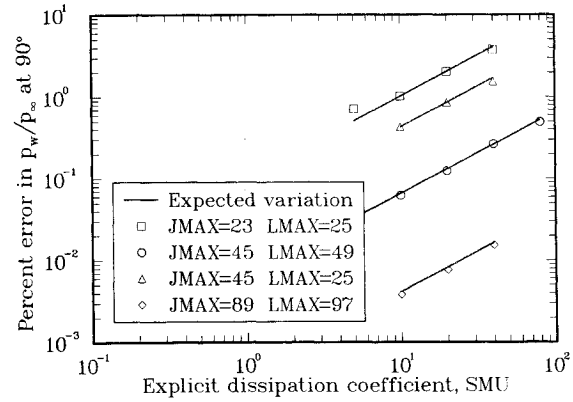

Fig. 3 Explicit dissipation factor, error in surface pressure p_w/p_∞ at 90 deg around the sphere as *SMU* is changed.

3) The error estimate can be used to determine if an appropriate distribution of grid points has been used.

The first item has been useful in discovering inaccuracies in the original difference scheme used in the NS3D code near the stagnation point. A difference scheme to avoid this problem is given in Ref. 6, and this problem was encountered originally by Widhopf and Victoria.[8] Grid refinement studies provide another check on the FORTRAN coding in a computational code.

Richardson extrapolation can be used in several forms with grid refinement for two-dimensional problems. The grid can be held fixed in one coordinate direction with the grid refined in the other coordinate direction, or the grid can be refined in both coordinate directions simultaneously. For a one-dimensional problem solved with an nth order numerical scheme, the exact solution Q_E can be expressed in terms of the numerical solution Q_N and the truncation errors as follows:

$$Q_E = Q_N + \alpha\Delta^n + \text{higher-order terms} \tag{23}$$

The coefficient α is to be determined from the numerical solutions. Numerical results are obtained with grid step-size Δ and 2Δ. With the higher-order terms neglected in the expression, these equations are combined to eliminate α and to obtain

$$Q_E = Q_N(\Delta) + [1/(2^n - 1)][Q_N(\Delta) - Q_N(2\Delta)] \tag{24}$$

This extrapolation provides a more accurate result where the truncation error is of higher order than in the numerical scheme. For the present second-order numerical scheme, the

exact solution is expressed as in Eq. (19). The numerical solutions are obtained on a series of grids where the number of grid points is doubled as the grid is refined. The number of grid points in each grid is related to the basic grid ($J_0 \times L_0$) by the relations $J_m - 1 = 2^m(J_0 - 1)$ and $L_m - 1 = 2^m(L_0 - 1)$, where $m = 0,1,2,3,\ldots$. The exact solution estimate when the grid is refined in the ξ coordinate direction and when L_m is held constant becomes

$$Q_E(J \to \infty) = Q_{N_m} + \tfrac{1}{3}(Q_{N_m} - Q_{N_{m-1}}) + \cdots \tag{25}$$

where the coefficient a in Eq. (19) is

$$a = \tfrac{1}{3}(Q_{N_m} - Q_{N_{m-1}})2^{2m} + \cdots$$

and by definition

$$Q_E(J \to \infty) = Q_E - b2^{-2m}$$

A similar relation is obtained when the grid is refined in the ζ direction and with the number of grid points J_m held constant. When the grid is refined in both coordinate directions, the exact solution is estimated from

$$Q_E = Q_{N_m} + \tfrac{1}{3}(Q_{N_m} - Q_{N_{m-1}}) + \cdots \tag{26}$$

and the error percentage of the dependent variables is determined from

$$\%\ \text{error of}\ Q_{N_m} = 100 \times [Q_{N_m} - Q_E]/Q_E \tag{27}$$

Numerical solutions have been obtained with the grid refined in one coordinate direction and the number of grid points held fixed in the other coordinate direction. Some of the results obtained from these solutions are tabulated in Tables B1-B6 in Appendix B. The influence of grid spacing on the surface pressure, shock-layer thickness, and heat flux at various values of ξ is given in these tables. The last column in each table is the extrapolated value obtained from the finest grid ($m = 2$) and next to finest grid ($m = 1$). This extrapolated value is used as the exact solution to estimate the accuracy of the numerical results with various numbers of grid points. The error in the surface pressure at various locations along the sphere is given in Fig. 4 as the grid is refined in the ξ coordinate along the body and in Fig. 5 as the grid is refined in the ζ coordinate direction across the shock layer. The results in Fig. 4 have good second-order behavior on all of the grids, whereas finer grids are required in Fig. 5 to obtain second-order behavior. The error in the surface heat flux at various locations along the sphere is given in Fig. 6 as the grid is refined in the ξ coordinate along the body and in Fig. 7 as the grid is refined in the ζ coordinate direction across the shock layer. The results in Fig. 7 have good second-order behavior on all the grids, whereas finer grids are required in Fig. 6 to obtain second-order behavior. The numerical results from NS3D appear to have second-order behavior when a sufficiently fine grid is employed.

Numerical results have been calculated on three grids where the number of grid points in each coordinate direction is doubled as the grid is refined. The coarse grid has $J = 23$ and $L = 25$, the medium grid has $J = 45$ and $L = 49$, and the fine

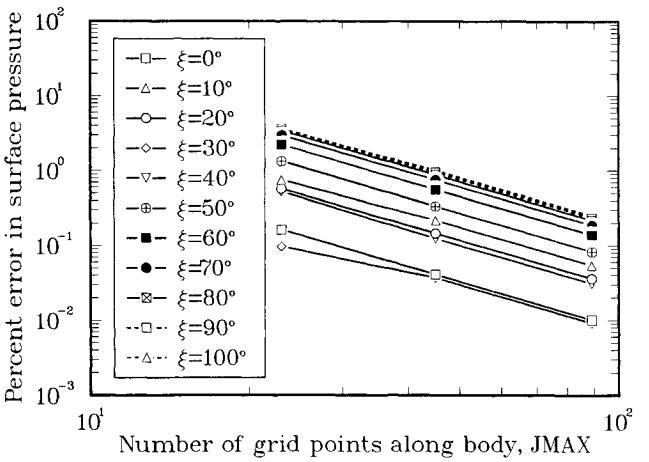

Fig. 4 Error in surface pressure p_w/p_∞ as grid is refined in the ξ direction.

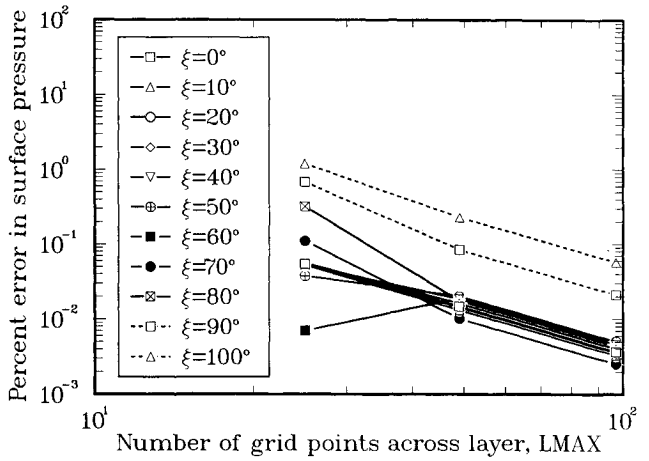

Fig. 5 Error in surface pressure p_w/p_∞ as grid is refined in the ζ direction.

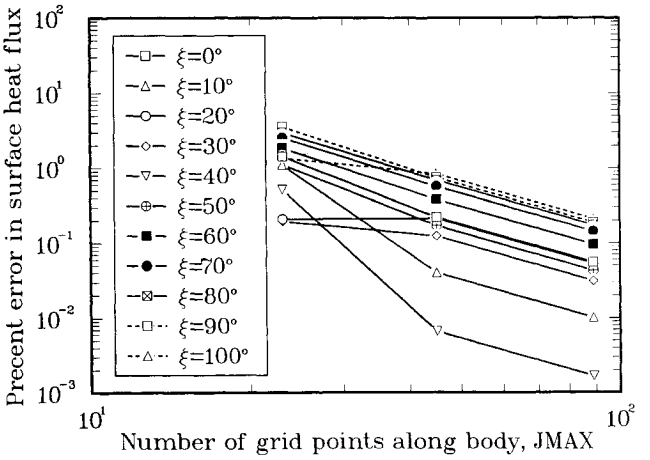

Fig. 6 Error in surface heat flux q as the grid is refined in the ξ direction.

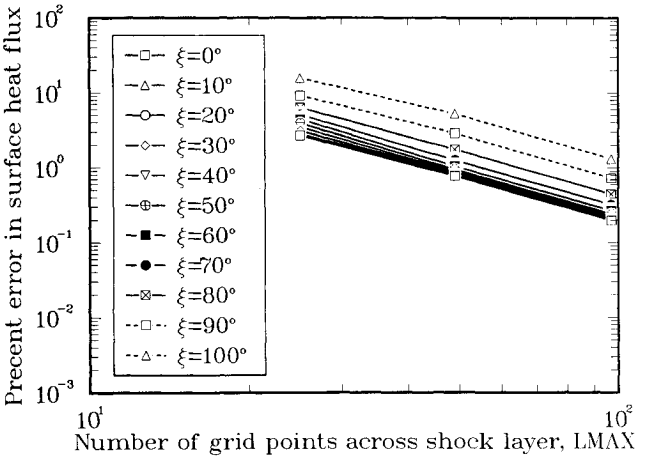

Fig. 7 Error in surface heat flux q as the grid is refined in the ζ direction.

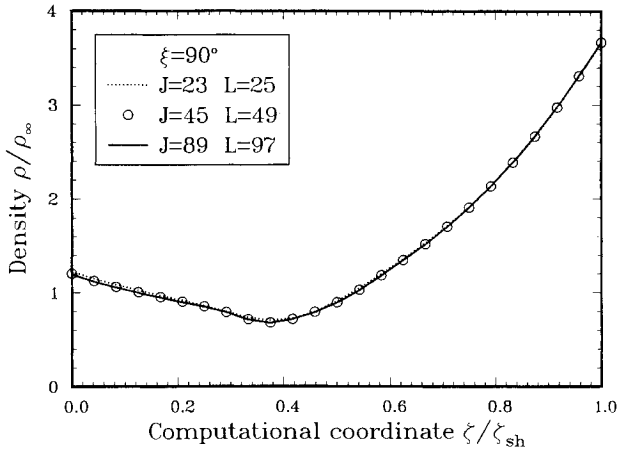

Fig. 8 Density ρ/ρ_∞ across shock layer at $\xi = 90$ deg for three grids.

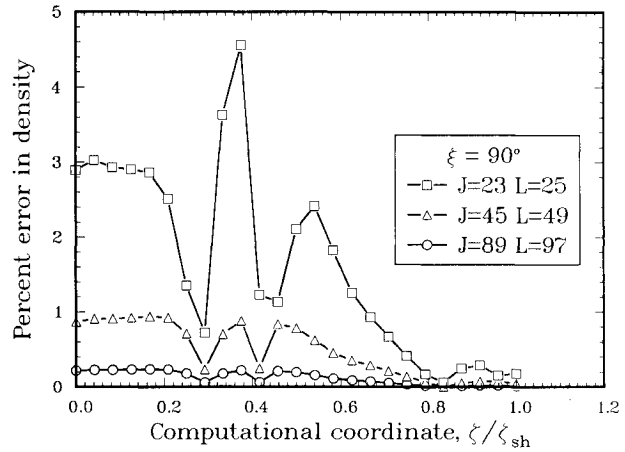

Fig. 9 Percent error in density ρ/ρ_∞ across shock layer at $\xi = 90$ deg as grid is refined in different coordinate directions: $J = 89$, $L = 97$.

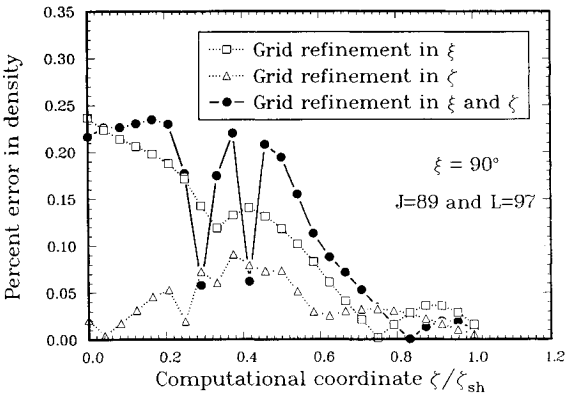

Fig. 10 Percent error in density ρ/ρ_∞ across shock layer at $\xi = 90$ deg as grid is refined in different coordinate directions: $J = 89$, $L = 97$.

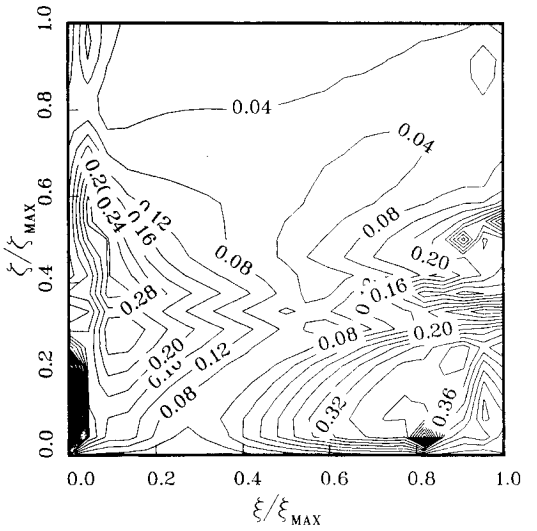

Fig. 11 Local total rms error throughout the flowfield shown in terms of the computational coordinates.

grid has $J = 89$ and $L = 97$. The coarse grid is illustrated in Fig. 1. The estimated exact solution at the grid points has been obtained with Richardson's extrapolation from Eq. (26). The accuracy of the dependent variables $Q = [\rho \ \rho u \ \rho w \ e]^T$ has been determined for the three grids and at all the grid points corresponding to the coarse grid. Presentation of this large amount of information in a useful form is considered now. The density dependent variable $Q_1 = \rho/\rho_\infty$ is used to illustrate the results across the shock layer at $\xi = 90$ deg for the three grids in Fig. 8. The results are presented in terms of the computational coordinate in order to see the behavior in the boundary-layer region. The dependence of the solution on the grid is noticeable for the coarse grid result; however, *the solution is never grid independent.* The error of the density for the three grids is given in Fig. 9. The error of the dependent variables decreases approximately by a factor of four for each grid refinement. The largest errors are occurring in the boundary-layer part of the flow, which indicates that a better distribution of grid points is possible. Grid refinement in one coordinate direction has been performed to determine which coordinate direction is producing the most error. A sample of these results is given in Fig. 10 for the density error with the finest grid. This result indicates a major part of the error is coming from too coarse a grid along the body (ξ direction). Also, the largest errors are located within the boundary-layer flow. This is only a sample of the type of information that is available from the error analysis. The density error throughout the flowfield can be illustrated with contour plots in black and white or in color. All of the preceding figures can be generated for each of the dependent variables. This large amount of information is useful and sometimes necessary to obtain an understanding of where the errors are occurring in the solution. An approach to reduce the number of error plots required to evalute the solution accuracy is to define the local total root mean square (rms) error as

$$E = \left(\sum_{n=1}^{N} (e^n)^2 / N \right)^{1/2} \tag{28}$$

The error or each dependent variable Q_n is obtained from Eq. (27) and is denoted with e^n, where $n = 1,2,\ldots, N$ and N is the total number of dependent variables. For each grid used in the grid refinement study, a figure with the local rms error can be generated. An example of this type of solution error analysis is given in Fig. 11 using the fine grid. This figure again shows that the largest solution errors are occurring in the boundary layer region ($\zeta/\zeta_{sh} < 0.4$), and the largest errors occur near the wall at the stagnation point and 90 deg ($\xi/\xi_{MAX} = 0.82$) along the sphere. At the stagnation point and near the wall, the momentum ρu is nearly zero, and large errors result from the extrapolation procedure used to obtain the solution along the body axis. Although the local total rms error is large at the body axis, the influence on the results of interest is small.

An approach to obtain one plot for the solution errors with the various grids is to define the global rms error at the interior grid points as

$$E_g = \left[\sum_{j=2}^{J-1} \sum_{l=2}^{L-1} \sum_{n=1}^{N} (e^n_{j,l})^2 / (J-2)(L-2)N \right]^{1/2} \tag{29}$$

The errors of the dependent variables are squared and summed over all of the interior grid points. This sum could include the boundary points, or the boundary points can be handled in a separate error term. The separation of the interior points from the boundary points allows an error analysis of the difference relations used to approximate the boundary conditions. The variation of the global rms error for the interior points with the three grids is given in Fig. 12 when the grid is refined by various approaches. These results show nearly second-order behavior for the three grids. The global rms error is reduced from 3% to approximately 0.2% as the grid is refined twice.

Richardson extrapolation has been used with the solution on the finest grid to provide slightly improved results for the surface pressure p_w/p_∞, shock layer thickness n_{sh}/D, and the surface heat flux q. These extrapolation results are presented in Table 3 at 10-deg increments around the sphere. The predictions in this table are the most accurate results that have been obtained in this study and are appropriate for a benchmark test case.

Comparison with Other Results

Very accurate numerical predictions of inviscid flow over spheres by Lyubimov and Rusanov[9] are compared with the NS3D code results in Table 3. The inviscid results are the second row at each ξ value. The present NS3D viscous predictions are at a sufficiently high Reynolds number that the predictions for shock-layer thickness and surface pressure are not expected to be significantly influenced by the viscous contributions. The influence of Reynolds number on the surface pressure has been evaluated by obtaining a solution with the NS3D code at a Reynolds number of 1.8875×10^8, where the boundary layer is an order of magnitude thinner. These results show that the pressure downstream on the sphere is slightly influenced by viscous effects; the higher Reynolds number solution gives a lower pressure in this region and is in closer agreement with the Euler predictions.

The contributions of the viscous terms in the thin-layer Navier-Stokes equations that are used in the NS3D code have been evaluated with results from a first-order boundary-layer code.[10] With a Reynolds number large enough that the boundary layer is thin compared to the shock-layer thickness, solutions from the boundary-layer equations at the stagnation point provide accurate flow properties near the wall. The boundary-layer solutions use Sutherland's viscosity law and constant Prandtl number as employed in the NS3D code. Any differences between accurate numerical predictions from the two codes result from the differences in the governing equations. The boundary-layer solution for the heat flux q requires the inviscid velocity gradient along the surface at the stagnation point, which has been obtained from inviscid numerical solutions.[9] With this velocity gradient, the heat flux q from the boundary-layer code has been determined; this result is given in Table 3 at the stagnation point ($\xi = 0$ deg).

Table 3 Extrapolated results from NS3D and inviscid results at various locations ξ around the sphere

ξ, deg	p_w/p_∞	n_{sh}/D	q, kW/m^2
0	32.6546	0.07898	107.572
	32.65[a]	0.0790[a]	106.81[b]
10	31.5241	0.08045	103.778
	31.52[a]	0.0805[a]	—
20	28.3396	0.08507	95.894
	28.33[a]	0.0850[a]	—
30	23.6661	0.09351	83.484
	23.66[a]	0.0935[a]	—
40	18.3054	0.10691	68.293
	18.28[a]	0.1070[a]	—
50	13.0846	0.12699	52.252
	13.06[a]	0.1270[a]	—
60	8.6363	0.15616	37.232
	8.603[a]	0.1560[a]	—
70	5.2679	0.19777	24.615
	5.227[a]	0.1975[a]	—
80	2.9754	0.25668	15.044
	2.931[a]	0.2565[a]	—
90	1.5609	0.34029	8.472
	1.506[a]	0.3400[a]	—
100	0.7651	0.46079	4.388

The experimental measurements of Widhopf and Hall[11] on a 9-deg sphere cone at Mach number 5 have been compared in Ref. 6 to the NS3D predictions for laminar flow over the sphere. The experimental flow conditions are those described in Table 1. The surface pressure predictions along the body are in good agreement with the measurements. The surface heat-flux measurements and predictions along the body are in reasonable agreement.

Accuracy of Governing Equations

As indicated in the preceding discussion, the code NS3D solves the thin-layer Navier-Stokes equations for a perfect gas. This approximate form of the Navier-Stokes equations neglects longitudinal curvature terms that occur in second-order boundary-layer theory. For the present case, where the boundary-layer thickness is small compared with the surface curvature in the longitudinal direction, the thin-layer Navier-Stokes are sufficiently accurate. The boundary conditions at the wall assume no slip or temperature jump, which is appropriate for the present case where the Reynolds number is sufficiently large. The shock wave is treated with the jump conditions across the shock wave obtained from the Rankine-Hugoniot relations.

The pressure is obtained from the perfect-gas relation $p = (\gamma - 1)\rho e_i$, which is obtained from the perfect-gas equation of state $p = \rho RT$ with the temperature determined from the perfect-gas relation $T = (\gamma - 1)e_i/R$. The validity of this relation is evaluated in Fig. 13 where the perfect gas relation is compared to results for equilibrium air at different densities. The density, ρ_0, is 1.29149 kg/m^3 at 1 atm and 273.15 K. Except for the high-density case, the perfect-gas relation is accurate if the temperature is less than 600 K. At higher temperatures, the vibrational energy of the molecules becomes important, and the internal energy can no longer be obtained from the perfect-gas relation $e_i = RT/(\gamma - 1)$. In addition, at temperatures above 2000 K, oxygen begins to dissociate and the molecular weight of air is no longer a constant in the equation of state.

The transport properties required in the code are the viscosity and thermal conductivity of air. The viscosity has been determined from Sutherland's law as given in Eq. (8). The accuracy of the viscosity is shown in Fig. 14 where the recommended values of Touloukian[12] are compared with Sutherland's law. At low and high temperatures, Sutherland's viscosity law is inadequate, but for temperatures between 100–2000 K, this relation is very accurate. The thermal conductivity is obtained from the relation $k = \mu c_p/Pr$ where the viscosity μ is obtained from Sutherland's law, the specific heat $c_p = \gamma R/(\gamma - 1)$, and the Prandtl number $Pr = 0.72$. The accu-

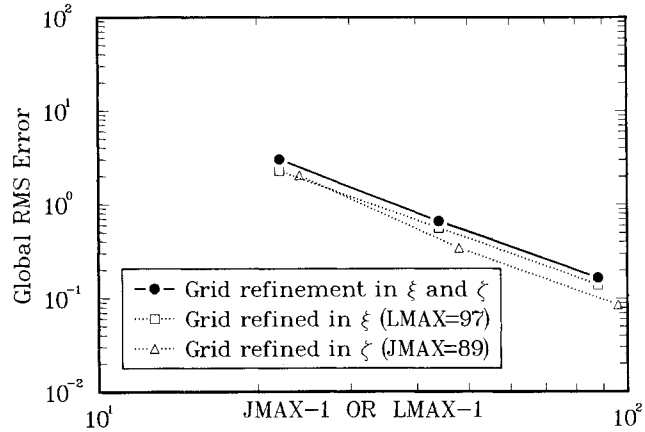

Fig. 12 Variation of the global rms error of the interior grid points as the grid is refined.

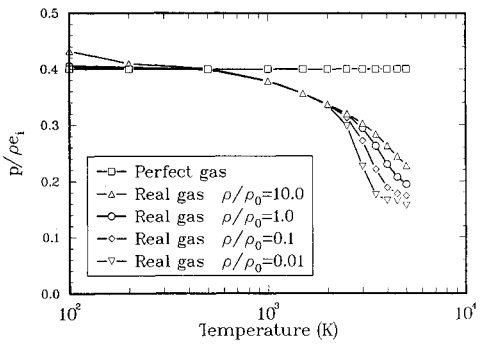

Fig. 13 Pressure correlation for real equilibrium air compared to perfect gas relation.

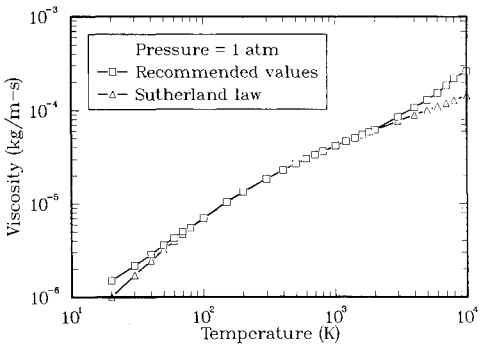

Fig. 14 Viscosity of air as a function of temperature at atmospheric pressure.

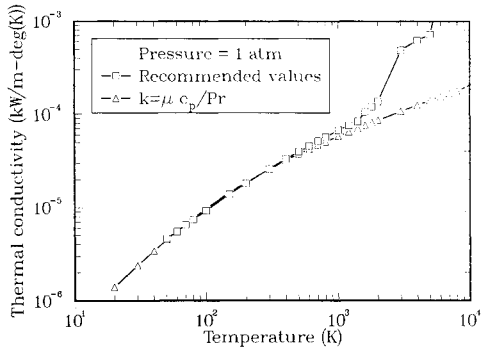

Fig. 15 Thermal conductivity of air as a function of temperature at atmospheric pressure.

racy of this thermal conductivity is shown in Fig. 15 with the recommended values of Touloukian.[12] The present thermal conductivity relation is appropriate for temperatures between 50–500 K.

The perfect-gas model with simplified transport properties is valid only for supersonic and hypersonic flow at low gas temperatures (100 K $< T <$ 500 K) as can occur in wind tunnels.

Summary and Recommendations

Code Verification—Solving Governing Equations Right

The influence on the numerical results of the explicit dissipation term added to the governing equations has been evaluated and shown to be unimportant when the finest grid ($J = 89$ and $L = 97$) is used. The grid refinement studies indicate the solutions have second-order convergence behavior on the finest grid but this is not always true on the coarse grids. Accuracy of the results on various grids has been determined where the exact solution is estimated with Richardson extrapolation. This approach has been used to improve the accuracy of the results obtained on the finest grid, and these results are presented in tabulated form as a benchmark test case. The estimated accuracy of the dependent variables at all grid points identifies the regions of the flowfield where solution errors are large and adjustment of the grid is needed. The present predictions for laminar flow are in very good agreement with other numerical results and experimental measurements.

Code Validation—Solving Right Governing Equations

The thin-layer Navier-Stokes equations with the perfect gas assumption, Sutherland's viscosity law, and constant Prandtl number appear to provide reasonably accurate predictions of blunt-body flows where the gas temperature is sufficiently low ($\lesssim$ 500 K). More complete models for the gas transport properties and pressure equation would extend the range of validity of the governing equations. This type of extension requires the assumption of vibrational equilibrium of the gas model. The quality of the experimental data needs to be improved to provide a more accurate evaluation of the modeling employed in numerical codes.

Comments and Recommendations

The solution of two-dimensional flows without an estimate of the numerical accuracy is rapidly becoming unsuitable. Solutions on several grids (or some other approach) will become part of the solution strategy with the accuracy of the results being part of the output from the code. The use of several grids could perhaps be combined into a solution procedures where the iteration method would include multigrid and adaptive grid techniques in a combined approach. More attention must be given to grid convergence properties of the numerical schemes so that the order of convergence is obtained over a wide range of grid spacings. Accuracy of numerical solutions of flows with captured shock waves must also be addressed.

Appendix A: Grid Across Shock Layer

Table A1 Grid distribution function

l	N_l	l	N_l
1	0.0000E+00	14	0.1704E+00
2	0.2049E−03	15	0.2426E+00
3	0.4430E−03	16	0.3184E+00
4	0.7609E−03	17	0.3941E+00
5	0.1240E−02	18	0.4698E+00
6	0.2034E−02	19	0.5456E+00
7	0.3453E−02	20	0.6213E+00
8	0.6102E−02	21	0.6971E+00
9	0.1113E−01	22	0.7728E+00
10	0.2057E−01	23	0.8485E+00
11	0.3757E−01	24	0.9243E+00
12	0.6620E−01	25	0.1000E+01
13	0.1102E+00	—	—

Appendix B: Calculations from NS3D Code

Table B1 Influence of J on surface pressure p_w/p_∞ at various ξ around sphere[a]

ξ, deg	$J = 23$	$J = 45$	$J = 89$	$J \to \infty$
0	32.60271	32.64244	32.65243	32.6558
10	31.28976	31.45670	31.50801	31.5251
20	28.17982	28.29943	28.33033	28.3406
30	23.64420	23.65836	23.66489	23.6671
40	18.40134	18.32903	18.31196	18.3063
50	13.25930	13.12889	13.09614	13.0852
60	8.82724	8.68491	8.64876	8.6367
70	5.42320	5.30760	5.27794	5.2681
80	3.07612	3.00139	2.98180	2.9753
90	1.61659	1.57537	1.56427	1.5606
100	0.79205	0.77233	0.76656	0.7646

[a] $L = 97$.

Table B2 Influence of L on surface pressure p_w/p_∞ at various ξ around sphere[a]

ξ, deg	$L=25$	$L=49$	$L=97$	$L\to\infty$
0	32.66891	32.65604	32.65243	32.6512
10	31.52343	31.51112	31.50801	31.5070
20	28.34461	28.33337	28.33033	28.3293
30	23.67707	23.66775	23.66489	23.6639
40	18.32079	18.31449	18.31196	18.3111
50	13.10039	13.09811	13.09614	13.0955
60	8.64775	8.64998	8.64876	8.6484
70	5.27201	5.27834	5.27794	5.2778
80	2.97245	2.98141	2.98180	2.9819
90	1.55396	1.56328	1.56427	1.5646
100	0.75782	0.76524	0.76656	0.7670

[a]$J=89$.

Table B3 Influence of J on shock layer thickness n_{sh}/D at various ξ around sphere[a]

ξ, deg	$J=23$	$J=45$	$J=89$	$J\to\infty$
0	0.08094	0.07947	0.07910	0.0790
10	0.08205	0.08083	0.08054	0.0804
20	0.08654	0.08542	0.08516	0.0851
30	0.09498	0.09386	0.09359	0.0935
40	0.10846	0.10727	0.10700	0.1069
50	0.12864	0.12737	0.12708	0.1270
60	0.15791	0.15655	0.15626	0.1562
70	0.19961	0.19818	0.19788	0.1978
80	0.25857	0.25710	0.25679	0.2567
90	0.34219	0.34070	0.34041	0.3403
100	0.46249	0.46116	0.46091	0.4608

[a]$L=97$.

Table B4 Influence of L on shock layer thickness n_{sh}/D at various ξ around sphere[a]

ξ, deg	$L=25$	$L=49$	$L=97$	$L\to\infty$
0	0.07901	0.07909	0.07910	0.0791
10	0.08046	0.08053	0.08054	0.0805
20	0.08507	0.08515	0.08516	0.0852
30	0.09350	0.09359	0.09359	0.0936
40	0.10690	0.10699	0.10700	0.1070
50	0.12699	0.12708	0.12708	0.1271
60	0.15617	0.15626	0.15626	0.1563
70	0.19781	0.19789	0.19788	0.1979
80	0.25678	0.25682	0.25679	0.2568
90	0.34052	0.34047	0.34041	0.3404
100	0.46127	0.46102	0.46091	0.4609

[a]$J=89$.

Table B5 Influence of J on heat flux q (kW/m^2) at various ξ around sphere[a]

ξ, deg	$J=23$	$J=45$	$J=89$	$J\to\infty$
0	108.89906	107.59688	107.41949	107.3604
10	104.71163	103.52755	103.55881	103.5692
20	95.89539	95.49354	95.64585	95.6966
30	83.46687	83.20159	83.27927	83.3052
40	68.49249	68.13511	68.13849	68.1396
50	52.70867	52.21511	52.14845	52.1262
60	37.82389	37.27447	37.16833	37.1329
70	25.16030	24.67574	24.57074	24.5357
80	15.42346	15.08090	15.00319	14.9773
90	8.70938	8.47350	8.42615	8.4104
100	4.27123	4.36645	4.33914	4.3300

[a]$L=97$.

Table B6 Influence of L on heat flux q (kW/m^2) at various ξ around sphere[a]

ξ, deg	$L=25$	$L=49$	$L=97$	$L\to\infty$
0	104.72245	106.78428	107.41949	107.6312
10	100.95110	102.93322	103.55881	103.7673
20	93.10041	95.05326	95.64585	95.8434
30	80.84852	82.74309	83.27927	83.4580
40	65.90934	67.67746	68.13849	68.2922
50	50.22207	51.77180	52.14845	52.2740
60	35.61830	36.87113	37.16833	37.2674
70	23.39515	24.33413	24.57074	24.6496
80	14.11606	14.80178	15.00319	15.0703
90	7.70679	8.24044	8.42615	8.4881
100	3.70637	4.16482	4.33914	4.3972

[a]$J=89$.

Acknowledgment

This work, performed at Sandia National Laboratories, was supported by the U.S. Department of Energy under Contract DE-AC04-76DP00789.

References

[1]*Validation of Computational Fluid Dynamics,* Vol. 1, Symposium Papers and Round Table Discussion, AGARD CP-437, Dec. 1988, p. RTD-10.

[2]Bradley, R. G., "CFD Validation Philosopy," *Validation of Computational Fluid Dynamics,* Vol. 1, Symposium Papers and Round Table Discussion, AGARD CP-437, Dec. 1988, pp. 1-1 to 1-6.

[3]*IEEE Standard Glossary of Software Engineering Terminology,* Inst. of Electrical and Electronics Engineers, New York, IEEE-STD-729-1983, 1983, p. 37.

[4]Boehm, B., *Software Engineering Economics,* Prentice-Hall, Englewood Cliffs, NJ, 1982, p. 728.

[5]Blottner, F. G., and Larson, D. E., "Navier-Stokes Code NS3D for Blunt Bodies Part I: Analysis, Results, and Verification," Sandia National Labs., Albuquerque, NM, SAND88-0504/1, March 1988.

[6]Blottner, F. G., "Verification of a Navier-Stokes Code for Solving the Hypersonic Blunt Body Problem," *Fourth Symposium on Numerical and Physical Aspects of Aerodynamic Flows,* California State Univ., Long Beach, CA, Jan. 1989, pp. 16–19.

[7]Richardson, L. F., and Gaunt, J. A., "The Deferred Approach to the Limit," *Transactions of the Royal Society of London,* Series A, Vol. 226, 1927, pp. 299–361.

[8]Widhopf, G. F., and Victoria, K. J., "On the Solution of the Unsteady Navier-Stokes Equations Including Multicomponent Finite Rate Chemistry," *Computers and Fluids,* Vol. 1, 1973, pp. 159–184.

[9]Lyubimov, A. N., and Rusanov, V. V., "Gas Flow Past Blunt Bodies, Part II: Tables of the Gasdynamic Functions," NASA TT F-715, Feb. 1973.

[10]Blottner, F. G., "Introduction to Computational Techniques for Boundary Layers," Sandia National Labs., Albuquerque, NM, SAND79-0893, Sept. 1979.

[11]Widhopf, G. F. and Hall, R., "Transitional and Turbulent Heat-Transfer Measurements on a Yawed Blunt Conical Nosetip," *AIAA Journal,* Vol. 10, No. 10, 1972, pp. 1318–1325.

[12]Touloukian, Y. S. (ed.), *Thermophysical Properties of Matter,* The TPRC Data Series, Plenum, New York, 1975, pp. 512, 611.

Clark H. Lewis
Associate Editor